Pseudomagnetic fields for sound at the nanoscale

Christian Brendel[a,b,1], Vittorio Peano[a,c], Oskar J. Painter[d,e,f], and Florian Marquardt[a,b]

[a]Institute for Theoretical Physics, University of Erlangen-Nürnberg, 91058 Erlangen, Germany; [b]Max Planck Institute for the Science of Light, 91058 Erlangen, Germany; [c]Department of Physics, University of Malta, Msida MSD 2080, Malta; [d]Kavli Nanoscience Institute, California Institute of Technology, Pasadena, CA 91125; [e]Institute for Quantum Information and Matter, California Institute of Technology, Pasadena, CA 91125; and [f]Thomas J. Watson, Sr. Laboratories of Applied Physics, California Institute of Technology, Pasadena, CA 91125

Edited by Tom C. Lubensky, University of Pennsylvania, Philadelphia, PA, and approved March 10, 2017 (received for review September 27, 2016)

There is a growing effort in creating chiral transport of sound waves. However, most approaches so far have been confined to the macroscopic scale. Here, we propose an approach suitable to the nanoscale that is based on pseudomagnetic fields. These pseudomagnetic fields for sound waves are the analogue of what electrons experience in strained graphene. In our proposal, they are created by simple geometrical modifications of an existing and experimentally proven phononic crystal design, the snowflake crystal. This platform is robust, scalable, and well-suited for a variety of excitation and readout mechanisms, among them optomechanical approaches.

nanomechanics | pseudomagnetic field | topological physics | optomechanics | phononic crystal

Unlike electrons, phonons do not feel a magnetic field, because they are not charged. As a consequence, much of the interesting physics connected to the behavior of charged particles in a magnetic field is absent for phonons, be it the Lorentz force or the unidirectional transport along the edges of the sample. In the past two years, researchers have started to study how one might make sound waves behave in ways similar to electrons in a magnetic field or related topological settings. This research promises to pave the way toward transport along edge channels that are either purely unidirectional (1) or helical (2) (i.e., with two "spins" moving in opposite directions), as well as the design of novel zero-frequency boundary modes (3, 4). The first few experimental realizations (1, 2, 4–8) and a number of theoretical proposals (3, 9–18) involve macroscopic setups. These include coupled spring systems (1, 2, 11–13, 19) and circulating fluids (9, 10, 16, 20); for a review see ref. 21. These designs represent important proof-of-principle demonstrations of topological acoustics and could open the door to useful applications at the macroscopic scale. However, they are not easily transferred to the nanoscale, which would be even more important for potential applications. First concepts for Chern insulators or topological insulators at the nanoscale are challenging and have not yet been implemented, because they require either strong laser driving (22) or designs that are hard to fabricate (23).

Fruitful inspiration for an entirely different avenue toward nonreciprocal transport can be found in the physics of electrons propagating on the curved surface of carbon nanotubes (24) and in strained graphene (25–28). It has been discovered that these electrons experience so-called pseudomagnetic fields, whose distribution depends on the strain pattern. Pseudomagnetic fields mimic real magnetic fields but have opposite sign in the two valleys of the graphene band structure and, thus, do not break time-reversal symmetry. This results in helical transport, with two counterpropagating species of excitations. In the past, this concept has already been successfully transferred to engineered carbon monoxide molecular graphene (29) and a photonic waveguide system (30). The idea of pseudomagnetic fields generated by distortions is so powerful because it can be implemented entirely using a purely geometrical approach, without any external driving, which is a crucial advantage at the nanoscale.

In this paper, we show how to engineer pseudomagnetic fields for sound waves at the nanoscale. In addition, it turns out that our design will be realizable in a platform that has already been fabricated and reliably operated in experiments, the snowflake phononic crystal (31). That platform has the added benefit of being a well-studied optomechanical system, which, as we will show, can also provide powerful means of excitation and readout. Besides presenting our nanoscale design we also put forward a general approach to pseudomagnetic fields for Dirac quasiparticles based on the smooth breaking of the appropriate point group (the $\mathcal{C}_6$ or the $\mathcal{C}_{3v}$ groups) and translational symmetries. Our scheme is especially well-suited to patterned engineered materials such as phononic and photonic crystals. It ties into the general efforts of steering sound in acoustic metamaterials at all scales (32–35).

Results

Dirac Equation and Gauge Fields. The 2D Dirac Hamiltonian in the presence of a gauge field $\mathbf{A}(\mathbf{x})$ reads (we set the Planck constant and the charge equal to one) (36)

$$\hat{H}_D = m\hat{\sigma}_z + v(p_x - A_x(\mathbf{x}))\hat{\sigma}_x + v(p_y - A_y(\mathbf{x}))\hat{\sigma}_y. \quad [1]$$

Here, m is the mass, v is the Dirac velocity, and $\hat{\sigma}_{x,y,z}$ are the Pauli matrices. For zero mass and a constant gauge field ($m = 0$ and $\mathbf{A}(\mathbf{x}) = \mathbf{A}$), the band structure forms a Dirac (double) cone, where the top and bottom cones touch at the momentum $\mathbf{p} = \mathbf{A}$.

In a condensed matter setting, the Dirac Hamiltonian describes the dynamics of a particle in a honeycomb lattice, or certain other periodic potentials, within a quasimomentum valley (i.e., within the vicinity of a lattice high-symmetry point in the Brillouin zone). In this context, $\mathbf{p}$ is the quasi-momentum counted off from the relevant high-symmetry point. Here, we are interested in a scenario where the Dirac Hamiltonian Eq. **1** is defined in two different valleys mapped into each other via the time-reversal symmetry operator $\mathcal{T}$. This scenario is realized in

Significance

Unlike electrons, phonons do not feel a magnetic field, because they are not charged. Thus, much of the physics connected with charged particles in magnetic fields is absent for phonons, be it the Lorentz force or the unidirectional transport along the sample edges. Recently, researchers have started to study how one might make phonons akin to electrons in a magnetic field or related topological settings. The first experimental implementations involving coupled pendula or gyroscopes or air currents have already been realized at the macroscopic scale. Here, we describe a design that is well-suited for the nanoscale. It is purely geometric in nature and could be implemented based on an already experimentally demonstrated platform, a simple patterned 2D material.

Author contributions: V.P., O.J.P., and F.M. designed research; C.B., V.P., and F.M. performed research; C.B., V.P., and F.M. analyzed data; and C.B., V.P., O.J.P., and F.M. wrote the paper.

The authors declare no conflict of interest.

This article is a PNAS Direct Submission.

[1]To whom correspondence should be addressed. Email: christian.brendel@mpl.mpg.de.

This article contains supporting information online at www.pnas.org/lookup/suppl/doi:10.1073/pnas.1615503114/-/DCSupplemental.

graphene, where the Dirac equation is defined in the two valleys around the symmetry points **K** and **K′**. For charged particles, the gauge field $\mathbf{A}(\mathbf{x})$ usually describes a real magnetic field **B**, where $\mathbf{B} = \nabla \times \mathbf{A}$. In this case, the time-reversal symmetry $\mathcal{T}$ is broken. For $m = 0$ and a constant magnetic field, the Dirac cones break up in a series of flat Landau levels (36),

$$E_n = \text{sign}(n)\sqrt{|n|}\omega_c, \quad \omega_c = v\sqrt{2B}, \qquad [2]$$

where $n \in Z$ and ω_c is the cyclotron frequency. The presence of a physical edge then leads to topologically protected gapless edge states in each valley. For a real magnetic field, the edge states in the two valleys have the same chirality. However, here, we will be interested in the case of engineered pseudomagnetic fields, where the gauge field $\mathbf{A}(\mathbf{x})$ does not break the $\mathcal{T}$-symmetry. In this case, $\mathbf{B} = \nabla \times \mathbf{A}$ must have opposite sign in the two different valleys to preserve the $\mathcal{T}$-symmetry. It is clear that as long as one can focus on a single valley, the nature of the magnetic field (real or pseudo magnetic field) does not play any role. This holds true also in the presence of boundaries. For a given valley and gauge potential **A**, exactly the same edge excitations will emerge in the presence of a pseudo or a real magnetic field. The nature of the magnetic field only becomes apparent when the eigenstates belonging to inequivalent valleys are compared. When time-reversal is preserved (pseudomagnetic field), each edge state in one valley has a time-reversed partner with opposite velocity in the other valley. Thus, the edge states induced by a pseudomagnetic field are not chiral but rather helical.

Dirac Phonons in the Snowflake Phononic Crystal. Finite element method (FEM) mechanical simulations of a silicon thin-film snowflake crystal are presented in Fig. 1. Throughout this paper, we restrict our attention to the modes that are even under the mirror symmetry $(x, y, z) \to (x, y, -z)$, that is, the z-symmetric modes (*SI Appendix*). The mechanical band structure is shown in Fig. 1*C*. It features a large number of Dirac cones at the high-symmetry point **K**. Each cone has a time-reversed partner at the point **K′** (not shown). These pairs of Dirac cones are robust structures: When the radius of the snowflake is varied, they are shifted in energy (and can possibly cross other bands) but the top and bottom cones always touch at the corresponding high-symmetry point (Fig. 1*C*). In other words, the mass m and the gauge field **A** are always zero in the corresponding Dirac Hamiltonian. To generate the desired gauge field, it is necessary to modify the pattern of holes in a way that breaks the symmetries of the crystal (see below).

In preparation of this, we use the snowflake radius as a knob to engineer a pair of Dirac cones that are spectrally well-isolated from other bands and have a large velocity. The snowflake crystal can be viewed as being formed by an array of triangular membranes arranged on a honeycomb lattice and connected through links (Fig. 1*B*). In principle, we could choose a situation where the links are narrow (large snowflake radius r), such that all of the groups of bands are spectrally well-isolated. However, then the Dirac velocities tend to be small. For wider links (smaller r), the motion of the adjacent edges of neighboring triangular membranes becomes strongly coupled. This gives rise to normal modes where such adjacent sides oscillate in phase, resulting in large displacements of the links. We note that these links are arranged on a Kagome lattice (Fig. 1*A*). This observation explains the emergence (see $r = 180$ nm plot of Fig. 1*E*) of a group of three bands, separated from the remaining bands by complete band gaps, and supporting large-velocity Dirac cones. The triplet of isolated bands can be fitted well by a Kagome lattice tight-binding model with nearest-neighbor and next-nearest-neighbor hopping. The Kagome lattice model would be entirely sufficient to guide us in the engineering of the desired gauge fields. However, we prefer to pursue a more fundamental and general approach based on the symmetries of the underlying snowflake crystal.

Identifying the Dirac Pseudospin by the Symmetries. The snowflake thin-film slab crystal has $\mathcal{D}_{6h}$ point group symmetry. If we restrict

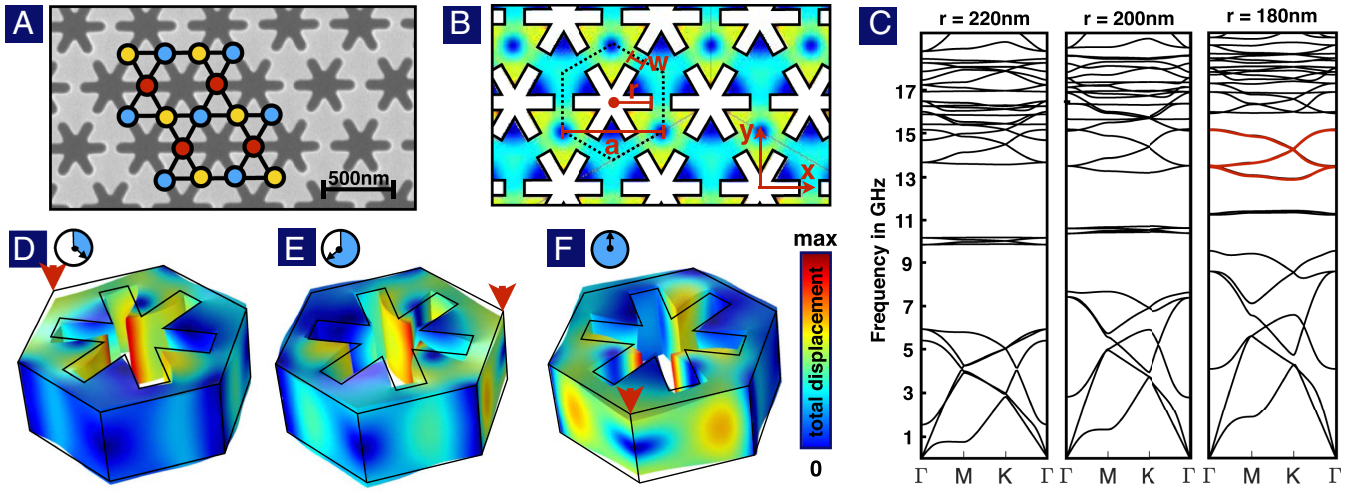

Fig. 1. Snowflake crystal: geometry, band structure, and displacement fields. (*A*) Image of a silicon snowflake phononic crystal. It is formed by upward and downward triangles connected by links. The links form a Kagome lattice whose Bravais sublattices are marked by circles of different colors. (*B*) Top view of the field $|\psi_{m_s,\tau}(\mathbf{x},z)|^2$ (time-averaged square displacement) for one normal mode at the Dirac point ($m_s = -1$ and valley $\tau = -1$). The dashed line indicates the border of the Wigner–Seitz cell. The relevant geometric parameters are indicated. (*C*) Phononic band structure (*z*-symmetric modes) for three values of the snowflake radius *r*, in silicon. For $r = 180$ nm, a group of three bands (plotted in red) is separated by complete band gaps from the remaining bands. The triplet can be fitted well by a Kagome lattice model and exhibits Dirac cones at the high symmetry points **K** and **K′** (only **K** is shown). At the cone tip, the degenerate normal modes have quasi-angular momentum $m_s = \pm 1$. (*D*–*F*) Snapshots of the mechanical displacement field (absolute value encoded in the color scale) for the mode with quasi-angular momentum $m_s = -1$ and valley $\tau = -1$, within a Wigner–Seitz cell. Subsequent snapshots are taken after one-third of a period (cf. the clocks). Each snapshot is the anticlockwise rotation by a $2\pi/3$ angle around the snowflake center of the previous snapshot (cf. the arrows). Movie S1 shows this dynamics in more detail. All band structures and normal mode profiles are computed using a finite-element solver (COMSOL). The simulated slab thickness is 220 nm. The snowflake spacing *a* and the width *w* (see *B*) are $(a, w) = (500, 75)$ nm. In *B*, *D*, *E*, and *F* the snowflake radius is $r = 180$ nm.

our attention to the z-symmetric modes, the remaining point group is $\mathcal{C}_{6v}$ (sixfold rotations about the snowflake center and mirror symmetries about the vertical planes containing a lattice basis vector). The degeneracies underpinning the Kagome Dirac cones as well as the other robust cones in Fig. 1*B* are usually referred to as essential degeneracies. They are preserved if the point group includes at least the $\mathcal{C}_6$ symmetries (sixfold rotational symmetry about the snowflake center) or the $\mathcal{C}_{3v}$ symmetries (threefold rotations and mirror symmetries about three vertical planes containing a lattice unit vector). The point group here contains both groups but, for concreteness, our explanation will focus on the $\mathcal{C}_6$ symmetry. It is useful to think of the $\mathcal{C}_6$ symmetry as a combination of a $\mathcal{C}_3$ (threefold) symmetry group and a $\mathcal{C}_2$ (twofold) symmetry group. The threefold rotations $\mathcal{C}_3$ belong to the group of the high-symmetry points **K** and **K**′ (they leave each of these points invariant modulo a reciprocal lattice vector). As a consequence, at these points, the eigenmodes can be chosen to be eigenvectors of the $\mathcal{C}_3$ rotations with quasi-angular momentum $m_s = 0, \pm 1$. The essential degeneracies come about because the eigenvectors with nonzero quasi-angular momentum m_s come in quadruplets (a degenerate pair in each inequivalent valley), mapped into each other via the time-reversal symmetry operator $\mathcal{T}$ and the rotation $\hat{R}(\pi)_z$ by 180° about the snowflake center (the sole nontrivial element of the $\mathcal{C}_2$ group). If we denote the members of a quadruplet by $\boldsymbol{\psi}_{m_s,\tau}(\mathbf{x}, z)$, where $m_s = \pm 1$ and $\tau = \pm 1$ indicates the valley and z is the vertical coordinate, we have

$$\boldsymbol{\psi}_{m_s,\tau} = \mathcal{T}\boldsymbol{\psi}_{-m_s,-\tau} = \hat{R}(\pi)_z\boldsymbol{\psi}_{m_s,-\tau} = \mathcal{T}\hat{R}(\pi)_z\boldsymbol{\psi}_{-m_s,\tau}.$$

Note that both $\mathcal{T}$ and $R(\pi)$ change the sign of the quasimomentum and, thus, of τ. However, only $\mathcal{T}$ changes the sign of the quasi-angular momentum.

The Dirac Hamiltonian [**1**] for a given valley τ is obtained by projecting the underlying elasticity equations onto a 2D Hilbert space spanned by the normal modes

$$\boldsymbol{\psi}_{\mathbf{p},m_s,\tau}(\mathbf{x}, z) = e^{i\mathbf{p}\cdot\mathbf{x}}\boldsymbol{\psi}_{m_s,\tau}(\mathbf{x}, z), \qquad [3]$$

and by identifying $-m_s = \pm 1$ with the eigenvalues of the $\hat{\sigma}_z$ matrix (*SI Appendix*). In other words, the quasi-angular momentum m_s plays the role of the Dirac pseudospin. A mass term is forbidden because states with equal quasi-momentum and opposite quasi-angular momentum are mapped into each other by the symmetry $\mathcal{T}\hat{R}(\pi)_z$, $\boldsymbol{\psi}_{\mathbf{p},m_s,\tau}(\mathbf{x}, z) = \mathcal{T}\hat{R}(\pi)_z\boldsymbol{\psi}_{\mathbf{p},-m_s,\tau}(\mathbf{x}, z)$. A gauge field **A** is also forbidden because it would couple states with different quasi-angular momentum at the symmetry point.

In our phononic Dirac system, the eigenstates $\boldsymbol{\psi}_{m_s,\tau}(\mathbf{x}, z)$ are 3D complex vector fields. They yield the displacement fields

$$\mathbf{u}_{m_s,\tau}(\mathbf{x}, z, \phi) = \mathrm{Re}[\exp(-i\phi)\boldsymbol{\psi}_{m_s,\tau}(\mathbf{x}, z)], \qquad [4]$$

where ϕ is the phase of the oscillation. In this classical setting, $|\boldsymbol{\psi}_{m_s,\tau}(\mathbf{x},z)|^2$ can be interpreted as the square displacement averaged over one period, $|\boldsymbol{\psi}_{m_s,\tau}(\mathbf{x}, z)|^2 = \pi^{-1}\int_0^{2\pi} d\phi |\mathbf{u}_{m_s,\tau}(\mathbf{x}, z, \phi)|^2$. We note that the field $|\boldsymbol{\psi}_{m_s,\tau}(\mathbf{x}, z)|^2$ is invariant under threefold rotations about three inequivalent rotocenters: the center of the snowflake and the centers of the downward and upwards triangles (Fig. 1*B*). Three snapshots of the instantaneous displacement field for the state with $m_s = -1$ and $\tau = -1$ are shown in Fig. 1 *D*–*F*. By definition of a quasi-angular momentum eigenstate with $m_s = -1$, when the phase ϕ varies by $2\pi/3$ (after one-third of a period), the instantaneous displacement field is simply rotated clockwise by the same angle. When the valley is known, the quasi-angular momentum (which here plays the role of the pseudospin) can be directly read off from a single snapshot based on the position of the nodal lines. For $m_s\tau = 1$ ($m_s\tau = -1$), they are located at the center of the downward (upward) triangles (Fig. 1 *B* and *D*–*F*). (For a detailed explanation see *SI Appendix*.) Below, we will take advantage of our insight into the symmetries of the pseudospin eigenstates to engineer a local force field which selectively excites unidirectional waves.

Pseudomagnetic Fields and Symmetry Breaking. A crucial step toward the engineering of a pseudomagnetic field is the implementation of a spatially constant vector potential **A** in a translationally invariant system. Afterward arbitrary magnetic field distributions can be generated straightforwardly by breaking the translational invariance smoothly.

A perturbation that breaks the $\mathcal{C}_3$ symmetry but preserves the $\mathcal{C}_2$ symmetry will simply shift the Dirac cones, without opening a gap (Fig. 2*C*). This can be identified with the appearance of a constant gauge field **A** in the Dirac Hamiltonian [**1**]. As such, the connection between changes in the microscopic structure of the phononic metamaterial and the resulting gauge field can be obtained from FEM simulations by extracting the quasimomentum shift of the Dirac cones. We emphasize that, in this context, **A** has the dimension of an inverse length.

In the snowflake phononic crystal, we can achieve the desired type of symmetry breaking (breaking $\mathcal{C}_3$ while preserving $\mathcal{C}_2$) by designing asymmetric snowflakes formed by arms of different lengths, r_1, r_2, r_3 (Fig. 2*A*). If only one of the arms is changed, symmetry requires that the vector potential **A** point along that arm, as shown in Fig. 2*D*. For the Dirac cones associated with the Kagome lattice, our FEM simulations show that the cone displacement grows linearly with the length changes, as long as these remain much smaller than the average arm length $r = (r_1 + r_2 + r_3)/3$. In this linear regime, and for a general combination of arm lengths, r_1, r_2, r_3, we have

$$\mathbf{A} \approx \tau f(r)\mathbf{d}, \quad \mathbf{d} = (r_1\mathbf{e}_1 + r_2\mathbf{e}_2 + r_3\mathbf{e}_3). \qquad [5]$$

The unit vectors $\mathbf{e}_j$ point into the direction of the corresponding snowflake arms, $\mathbf{e}_j = \cos\theta_j\mathbf{e}_x + \sin\theta_j\mathbf{e}_y$, where $\theta_j = 2\pi(j-1)/3$. The factor $\tau = \pm 1$ appears because we have not broken the time-reversal symmetry and, thus, the vector potential has opposite sign in the two valleys. We note that in general changes of the arm lengths also shift the frequency of the Dirac point. When the arm lengths are chosen to be position-dependent, as is required

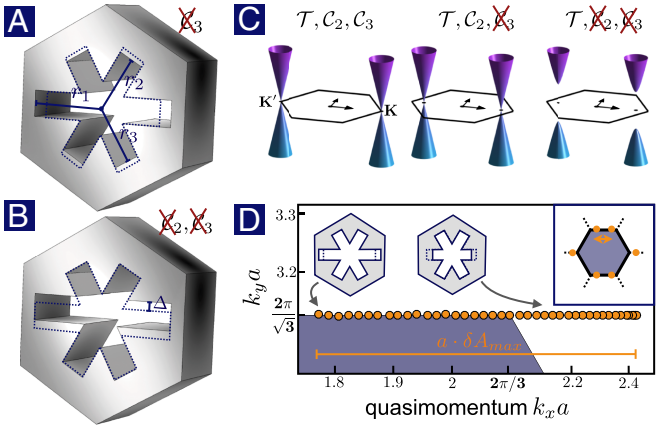

Fig. 2. Snowflake geometry and Dirac cones. (*A*) Geometry of the snowflake unit cell, depicting a situation with a broken threefold rotational symmetry $\mathcal{C}_3$ but preserved twofold rotational symmetry $\mathcal{C}_2$. (*B*) Geometry where both $\mathcal{C}_3$ and $\mathcal{C}_2$ symmetries are broken (a snowflake arm is displaced vertically by Δ). (*C*) Resulting shape of the Dirac cones. Breaking $\mathcal{C}_3$, while time-reversal symmetry $\mathcal{T}$ and $\mathcal{C}_2$ are maintained, leads to gapless cones displaced from the high-symmetry points. When also the $\mathcal{C}_2$ symmetry is broken, a band gap (mass) separating the upper and lower cones appears. (*D*) Displacement of the Dirac cone for the valley $\tau = -1$, for the geometry in *A* when r_1 is varied from 160 nm to 200 nm, while $r_2 = r_3$ and $r = (r_1 + r_2 + r_3)/3 = 180$ nm. The remaining parameters are as in Fig. 1.

for implementing arbitrary magnetic fields, this energy shift will enter the Dirac equation as a scalar potential $V(\mathbf{x})$, which may be unwanted. However, our numerical simulations show that we can keep $V(\mathbf{x})$ approximately constant, by retaining a constant average arm length r. Any smooth deviations from that are harmless as long as the resulting potential shifts remain much smaller than the typical gap between Landau levels, set by the cyclotron frequency ω_c, which is easily feasible. Nonsmooth disorder caused by fabrication imperfections requires a separate treatment (discussed below).

Phononic Landau Levels and Edge States in a Strip. We can test these concepts by implementing a constant phononic pseudomagnetic field in an infinite snowflake crystal strip, where we can directly test our simplified description against full microscopic simulations. The strip is of finite width W in the y-direction (where $-W/2 < y < W/2$). We can realize the corresponding vector potential in the Landau gauge, $\mathbf{A}(\mathbf{x}) = (-B_z y, 0, 0)$, by varying the length r_1 along the x axis, while keeping the remaining arm lengths equal, $r_2 = r_3$. For concreteness we choose $B_z > 0$ for $\tau = -1$.

The treatment of the boundaries merits special consideration. We recall that particles in pseudomagnetic fields are guaranteed to emulate their topologically protected counterparts (i.e., charged particles in real magnetic fields) only when the system parameters are varied smoothly such that no intervalley coupling is introduced. Clearly, sharp boundaries can lead to such undesired coupling. Indeed, it has been shown for graphene, in the case of real magnetic fields, that the edge states localized close to sharp armchair boundaries are not valley-polarized (37). Such valley mixing would arise also in the present system if sharp boundaries are chosen. Here, we address this challenge by engineering smooth boundaries. A notable advantage of our platform is that this task is completely straightforward. Any smooth gradient of snowflake parameters near the boundaries of the sample will lead to well-defined edge states that are spatially separated from the physical system boundary. In general, this could involve both a potential gradient as well as a gradient in the effective mass (gap). In our simulations, we will display results obtained for a smooth mass gradient, whose details do not matter for the qualitative behavior. This gives rise to magnetic edge states that can be easily addressed, because they have only negligible spatial overlap with their nonmagnetic counterparts. A Dirac mass term appears upon breaking the $\mathcal{C}_2$ symmetry, which we here choose to do by transversally displacing one of the snowflake arms, as shown in Fig. 2*B*, with the displacement varying smoothly in the interval $W_{\text{bulk}}/2 < |y| < W/2$.

By changing the snowflake arm lengths we can displace the Dirac cones only over a finite range of quasi-momenta. In our simulations $\delta A_{\max} \approx 0.17\pi/a$, as shown in Fig. 2*D*. Using Eq. **2** and the definition of the magnetic length $\ell_B = B^{-1/2}$, we see that there is a trade-off between the cyclotron frequency ω_c and, thus, the achievable magnetic band gaps and the system size in the appropriate magnetic units: $\omega_c \leq \sqrt{2} v \delta A_{\max}/w$, where $w = W/\ell_B$. For our FEM simulations we have chosen $w = 6.2$.

In Fig. 3 we display the phonon band structure and the phonon wave functions (mechanical displacement fields) extracted from finite-element numerical simulations as a function of the quasi-momentum k_x along the translationally invariant (infinite) direction. We display only positive k_x because, due to time-reversal symmetry, both the frequencies and the displacement fields are even functions of k_x. In the bulk, we expect to reproduce the well-known physics of Dirac materials in a constant (pseudo) magnetic field (36). Indeed, the numerically extracted band structure consists of a series of flat Landau levels at energies of precisely the predicted form $\omega = \bar{E} + E_n$ (E_n is defined in Eq. **2**; see Fig. 3*A* and *B*). The Landau plateaus extend over a quasi-momentum interval of width $\delta k_x \approx \delta A_{\text{bulk}} = W_{\text{bulk}} B$. Furthermore, in the bulk, we expect the mechanical eigenstates to be localized states of size $\ell_B = B^{-1/2}$ (in the y-direction). Their quasi-momentum k_x should be related to the position via $\bar{y} = -[k_x - 2\pi/(3a)]/B_z$. This behavior is clearly visible in Fig. 3*C*, where we show the displacement field of the central Landau level. A zoom-in of this field (Fig. 3*D*) reveals that, at the lattice scale, it displays the same intensity pattern as the bulk pseudospin eigenstate $m_s = -1$ shown previously in Fig. 1*F*. This behavior is also predicted by the effective Dirac description where the central Landau level is indeed a pseudospin eigenstate with $m_s = -1$ when the magnetic field B_z is positive (36). Note that the pseudomagnetic field engineered here also gives rise to a Lorentz force that will curve the trajectory of phonon wavepackets traveling in the bulk of the sample. The sign of the force is determined by the valley index τ.

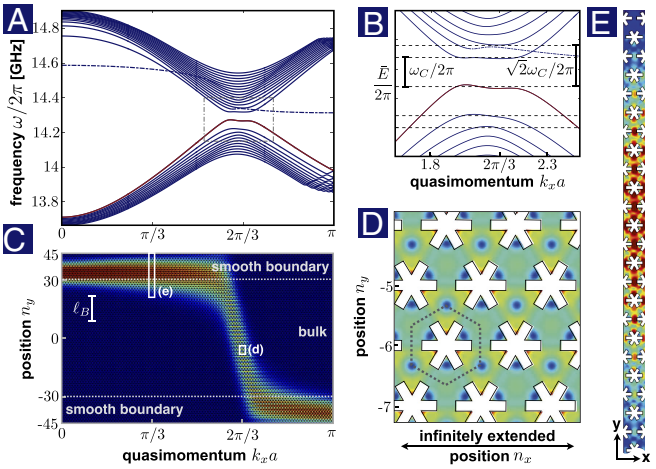

Fig. 3. Band structure and displacement fields of a strip in a constant pseudomagnetic field. (*A*) Band structure (only the *z*-symmetric modes are shown) and (*B*) zoom-in of the valley $\tau = -1$. The band structure displays multiple flat Landau plateaus in the vicinity of the **K′**-point ($k_x a = 2\pi/3$). In *B*, the dashed lines indicate the energies of the Landau levels as calculated from the Dirac equation for mass $m = 0$ (cf. Eq. **2**). In *A* and *B*, the dotted-dashed bands correspond to intrinsic nonchiral edge states located at the physical boundary of the system (*SI Appendix*). (*C*) Mode shape of the 0-th Landau level and the ensuing edge states (marked in red in *A* and *B*) as a function of the quasi-momentum k_x. The region of the smooth boundaries (where $m \neq 0$) is marked in gray and the magnetic length ℓ_B in white. (*D*) Zoom-in of the displacement field of the $n = 0$ Landau level. At the lattice scale, the displacement field pattern encodes the pseudospin $m_s = -1$ of the Landau level (cf. Fig. 1*B*). (*E*) Zoom-in of the edge state displacement field. The profile of the arm lengths r_i and of the displacement Δ are shown in *SI Appendix*, Fig. S3. The other parameters are the same as in Fig. 1.

Having demonstrated that we can implement a constant phononic pseudomagnetic field in the bulk, we now discuss the resulting physics at the boundary. Each Landau level gives rise to an edge state in the region of the smooth boundaries. The typical behavior of the wavefunction is shown (for $n = 0$) in Fig. 3*C*. For increasing quasi-momenta k_x, an edge state localized on the upper boundary smoothly evolves into a bulk state, and eventually into an edge state localized on the lower boundary. In this way, at any given energy, edge states always appear pairwise (at the upper and lower boundary), as is clear from Fig. 3 *A* and *B*. Although this may seem trivial, it is by no means what happens if we were to consider sharp boundaries. In fact, both for our system as well as for graphene in a pseudomagnetic field (28), sharp boundaries lead to a peculiar feature. In these cases, for zig-zag edges, there is a different number of edge states on the opposite sides of a strip. The two edges of the strip are not on equal footing because a pseudomagnetic field changes sign under a π-rotation. As a result, there is no uninterrupted edge state

around the sharp boundary of a finite-size sample (*SI Appendix*). This localization is induced by the intervalley coupling at the sharp edges and can be prevented by using smooth boundaries, leading to the robust behavior displayed in Fig. 3.

A characteristic feature of the band structure of a finite system with smooth boundaries in a pseudomagnetic field is that there is a band gap without edge states immediately below or above the $n=0$ Landau level (cf. Fig. 3 *A* and *B*). In our approach, the qualitative behavior of the edge states originating from the $n=0$ Landau level can be controlled by changing the sign of the mass. A negative mass (as in our simulations) drags this Landau level into the band gap below. Vice versa, a positive mass will drag it into the band gap above. This behavior is related to the peculiarity of the Landau level's being a pseudospin eigenstate (with $m_s=-1$) and, thus, an eigenstate of the mass term (with eigenvalue m) (cf. Eq. **1**).

Transport in a Finite Geometry and Disorder. Any pseudomagnetic field that is realized without explicit time-reversal symmetry breaking necessarily gives rise to helical transport, where the chirality depends on some artificial spin degree of freedom (i.e., the valley). A central question in this regard is the robustness against short-range disorder. To assess this, we have studied numerically transport in a finite geometry. As presented in Fig. 4, we consider a sample of hexagonal shape with smooth boundaries in the presence of a constant pseudomagnetic field (we choose the symmetric gauge for the vector potential A). In this illustrative example, a local probe drive excites vibrations near the boundaries, as indicated in Fig. 4*A*. Its frequency is chosen to lie inside the bulk band gap separating the $n=0$ and $n=-1$ Landau levels. In this band gap, the system supports a pair of counterpropagating helical edge states belonging to opposite valleys. One can select a propagation direction by engineering the driving force. In a simple setting, one could apply a time-dependent force that is engineered to excite only the pseudospin eigenstate $m_s=1$ in the valley $\tau=1$. This can be achieved by exerting forces at the three corners of a Wigner–Seitz cell, where the eigenstate displays a large vertical displacement (Fig. 1 *B–D*). There is a phase delay of $2\pi/3$ between any two corners, whereas a similar pattern of phase delays (but with opposite signs) occurs in the other valley. Thus, a force that is modulated with the right phase delays will selectively drive the valley $\tau=1$ and excite only excitations with a particular chirality.

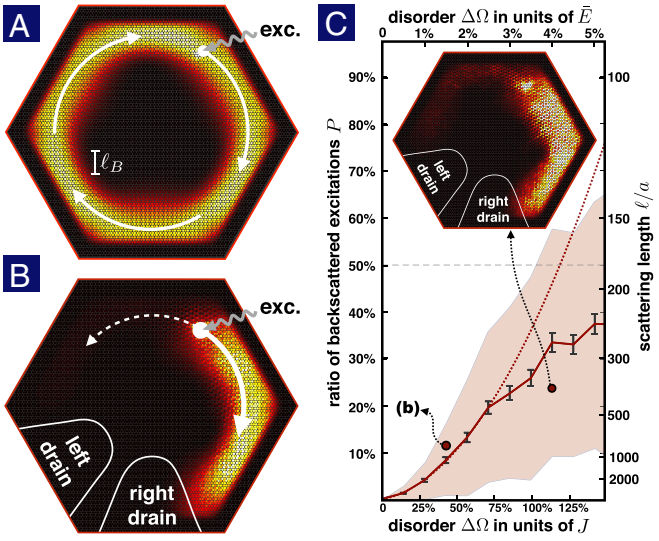

Fig. 4. Tight-binding transport simulations in a finite geometry: The hexagon (height, 55 unit cells) comprises an internal bulk area (height, 45 unit cells) and external smooth boundaries. An engineered oscillating force (at the position indicated by the gray arrow) with frequency in the middle of a band gap (separating the Landau levels $n=-1$ and $n=0$) launches clockwise propagating sound waves. (*A*) Resulting displacement field (unit-cell resolved). (*B* and *C*, *Inset*) Displacement field in the presence of disorder and drains where the excitation is absorbed. (*C*) Probability *P* (averaged over 150 disorder implementations) that an excitation is absorbed in the left drain as a function of the disorder strength. The estimated error is represented by error bars. The shaded area represents the values of *P* within one SD. In the tight-binding model, the random onsite energies are equally distributed on an interval of width $\Delta\Omega$. For weak disorder ($\Delta\Omega/J \lesssim 70\%$, where *J* is the average hopping rate), *P* can be fitted well by a parabola (dashed line), indicating that the transport is quasi-ballistic. In this regime, the corresponding scattering length ℓ is shown in the right vertical axis.

It turns out to be most efficient (and entirely sufficient) to implement the numerical simulations for these rather large finite-size geometries with the help of a tight-binding model on a Kagome lattice (*SI Appendix*). The parameters of that model can be matched to full FEM simulations that have been performed for the translationally invariant case. This allows us to systematically study the effects of disorder. In the presence of moderate levels of smooth disorder, which does not couple the two valleys, the nature of the underlying magnetic field (pseudo vs. real) will not manifest itself and the transport will largely be immune to backscattering. Here, we focus instead on lattice-scale disorder that can lead to scattering with large momentum transfer that couples the two valleys and thereby leads to backscattering. We emphasize that short-range disorder will, in practice, introduce backscattering in any purely geometric approach to acoustic helical transport. In particular, this also includes acoustic topological insulators, where generic disorder will break the unitary symmetry that ultimately protects the transport (38). To quantify the effect of lattice scale disorder, we consider a setup with two drains, one to the clockwise and one to the counterclockwise direction, as shown in Fig. 4*B*. In the absence of disorder, the vibrations travel clockwise (in this example) and are absorbed in the right drain; only very weak residual backscattering occurs at the sharp hexagon corners. In the presence of lattice-scale disorder, a portion of the excitations will be backscattered and subsequently reach the left drain. In Fig. 4*C* we plot the portion P of excitations absorbed in the left drain, averaged over a large number of disorder implementations, as a function of the disorder strength. In the regime of quasi-ballistic transport (for weak enough disorder), P is proportional to the backscattering rate. Thus, it scales as the square of the disorder amplitude and can be used to extract the scattering length ℓ: $P=d/\ell$, where d is the distance between source and drain. In current nanoscale snowflake crystal experiments (31), the fabrication-induced geometric disorder is on the order of 1% of the absolute mechanical frequency $\bar{E}$ which corresponds to 25% of the average hopping rate in the tight-binding model. In that case, our simulations indicate the resulting scattering lengths ℓ to be very large (of the order of more than 1,000 snowflake unit cells).

Discussion

We emphasize once more that one of the great practical advantages of the pseudomagnetic-field-based design put forward here is that it relies entirely on a simple geometry. Because time-reversal symmetry is not broken, there is no need for driving. This is in contrast to the first proposal for engineered chiral sound wave transport at the nanoscale (22), where a patterned slab illuminated by a laser realizes a Chern insulator for sound. The laser drive in ref. 22 breaks the time-reversal symmetry, enabling unidirectional topologically protected transport, but it also requires a suitable engineering of the wavefront and rather strong intensities. The other existing proposal for topologically protected sound transport in a 2D nanoscale lattice can do without driving, because it is based instead on a topological insulator (23). However, it involves a geometry that seems to be hard to fab-

ricate, in contrast to the design described here, which is based on an experimentally proven simple structure. In addition, of course, a major difference between the topological insulator and our pseudomagnetic field approach is that the present design offers access to the entire physics of the quantum Hall effect, such as spatially inhomogeneous magnetic field distributions or flat bulk Landau levels. The latter may become particularly interesting for situations with interactions between the excitations.

Because our design is scale-invariant, a variety of different implementations can be easily envisioned. At the nanoscale, the fabrication of thin-film silicon snowflake crystals and resonant cavities has already been demonstrated with optical readout and actuation (31). At the macroscale, the desired geometry could be realized using 3D laser printing and similar techniques. A remaining significant challenge relates to the selective excitation of helical sound waves and the subsequent readout. In an optomechanical setting, the helical sound waves can be launched by carefully crafting the applied radiation pressure force. For the typical dimensions of existing snowflake optomechanical devices operating in the telecom wavelength band (lattice spacing $a \approx 500$ nm), the required force could be engineered using tightly focused intensity-modulated laser beams impinging from above on three different snowflake triangles. The readout could occur by measuring motionally induced sidebands on the reflection of a laser beam. Although the direct radiation pressure of the beam will induce rather weak vibrations, they could still be resolved using optical heterodyning techniques. Alternatively, in a structure scaled up 10 times, selected triangles could host defect mode optical nanocavities. This would boost the radiation pressure force and the readout precision by the cavity finesse (*SI Appendix*). Helical sound waves can then be launched by either directly modulating the light intensity or a photon–phonon conversion scheme, using a strong red-detuned drive, with signal photons injected at resonance. In the micron regime one can benefit from electromechanical interactions. A thin film of conducting material deposited on top of the silicon slab in combination with a thin conducting needle pointing toward the desired triangles forms a capacitor. In this setting, an a.c. voltage would induce the required driving force. The vibrations could be read out in the same setup as they are imprinted in the currents through the needles. In a different electromechanical approach, the phononic crystal could be made out of a piezoelectric material and excitation and readout occur via piezoelectric transducers (39).

We have shown how to engineer pseudomagnetic fields for sound at the nanoscale purely by geometrical means in a well-established platform. Our approach is based on the smooth breaking of the $\mathcal{C}_6$ or the $\mathcal{C}_{3v}$ point groups and the discrete translational symmetry in a patterned material; it is, thus, of a very general nature and directly applies to photonic crystals as well. Indeed, the same geometrical modifications that have led to the pseudomagnetic fields for sound investigated in our work will also create pseudomagnetic fields for light (30, 38) in the same setup. Our approach offers a paradigm to design helical photonic and phononic waveguides based on pseudomagnetic fields. In addition to edge state transport, our approach allows for the design of arbitrary spatial distributions of pseudomagnetic fields, which could be used to study bulk phonon transport under the action of artificial Lorentz forces.

ACKNOWLEDGMENTS. This work was supported by European Research Council Starting Grant OPTOMECH (to V.P., C.B., and F.M.) and by the European Marie-Curie Innovative Training Network cQOM (F.M.). This project has received funding from the European Union's Horizon 2020 research and innovation programme under Grant 732894 (Hybrid Optomechanical Technologies) (to V.P. and F.M.). This work was also supported by the Air Force Office of Scientific Research–Multidisciplinary University Research Initiative (MURI) Quantum Photonic Matter, Army Research Office–MURI Quantum Opto-Mechanics with Atoms and Nanostructured Diamond Grant N00014-15- 1-2761, the Institute for Quantum Information and Matter, and NSF Physics Frontiers Center Grant PHY-1125565 with support of Gordon and Betty Moore Foundation Grant GBMF-2644 (all to O.J.P.).

1. Nash LM, et al. (2015) Topological mechanics of gyroscopic metamaterials. *Proc Natl Acad Sci USA* 112:14495–14500.
2. Süsstrunk R, Huber SD (2015) Observation of phononic helical edge states in a mechanical topological insulator. *Science* 349:47–50.
3. Kane CL, Lubensky TC (2013) Topological boundary modes in isostatic lattices. *Nat Phys* 10:39–45.
4. Paulose J, Chen BG-g, Vitelli V (2015) Topological modes bound to dislocations in mechanical metamaterials. *Nat Phys* 11:153–156.
5. Xiao M, et al. (2015) Geometric phase and band inversion in periodic acoustic systems. *Nat Phys* 11:240–244.
6. He C, et al. (2016) Acoustic topological insulator and robust one-way sound transport. *Nat Phys* 12:1124–1129.
7. Rocklin DZ, Zhou S, Sun K, Mao X (2017) Transformable topological mechanical metamaterials. *Nat Commun* 8:14201.
8. Chen BG-g, Upadhyaya N, Vitelli V (2014) Nonlinear conduction via solitons in a topological mechanical insulator. *Proc Natl Acad Sci USA* 111:13004–13009.
9. Yang Z, et al. (2015) Topological acoustics. *Phys Rev Lett* 114:114301.
10. Khanikaev AB, Fleury R, Mousavi SH, Alu A (2015) Topologically robust sound propagation in an angular-momentum-biased graphene-like resonator lattice. *Nat Commun* 6:8260.
11. Kariyado T, Hatsugai Y (2015) Manipulation of dirac cones in mechanical graphene. *Sci Rep* 5:18107.
12. Wang P, Lu L, Bertoldi K (2015) Topological phononic crystals with one-way elastic edge waves. *Phys Rev Lett* 115:104302.
13. Pal RK, Schaeffer M, Ruzzene M (2016) Helical edge states and topological phase transitions in phononic systems using bi-layered lattices. *J Appl Phys* 119:084305.
14. Fleury R, Khanikaev AB, Alu A (2016) Floquet topological insulators for sound. *Nat Commun* 7:11744.
15. Mei J, Chen Z-G, Wu Y (2016) Pseudo-time-reversal symmetry and topological edge states in two-dimensional acoustic crystals. *Sci Rep* 6:32752.
16. Chen Z-G, Wu Y (2016) Tunable topological phononic crystals. *Phys Rev Appl* 5:054021.
17. Rocklin DZ, Chen BG-g, Falk M, Vitelli V, Lubensky TC (2016) Mechanical Weyl modes in topological Maxwell lattices. *Phys Rev Lett* 116:135503.
18. Sussman DM, Stenull O, Lubensky TC (2016) Topological boundary modes in jammed matter. *Soft Matter* 12:6079–6087.
19. Prodan E, Prodan C (2009) Topological phonon modes and their role in dynamic instability of microtubules. *Phys Rev Lett* 103:248101.
20. Lu J, Qiu C, Ke M, Liu Z (2016) Valley vortex states in sonic crystals. *Phys Rev Lett* 116:093901.
21. Süsstrunk R, Huber SD (2016) Classification of topological phonons in linear mechanical metamaterials. *Proc Natl Acad Sci USA* 113:E4767–E4775.
22. Peano V, Brendel C, Schmidt M, Marquardt F (2015) Topological phases of sound and light. *Phys Rev X* 5:031011.
23. Mousavi SH, Khanikaev AB, Wang Z (2015) Topologically protected elastic waves in phononic metamaterials. *Nat Commun* 6:8682.
24. Kane CL, Mele EJ (1997) Size, shape, and low energy electronic structure of carbon nanotubes. *Phys Rev Lett* 78:1932–1935.
25. Mañes JL (2007) Symmetry-based approach to electron-phonon interactions in graphene. *Phys Rev B* 76:045430.
26. Guinea F, Katsnelson MI, Geim AK (2010) Energy gaps and a zero-field quantum hall effect in graphene by strain engineering. *Nat Phys* 6:30–33.
27. Levy N, et al. (2010) Strain-induced pseudo–magnetic fields greater than 300 tesla in graphene nanobubbles. *Science* 329:544–547.
28. Low T, Guinea F (2010) Strain-induced pseudomagnetic field for novel graphene electronics. *Nano Lett* 10:3551–3554.
29. Gomes KK, Mar W, Ko W, Guinea F, Manoharan HC (2012) Designer dirac fermions and topological phases in molecular graphene. *Nature* 483:306–310.
30. Rechtsman MC, et al. (2013) Strain-induced pseudomagnetic field and photonic landau levels in dielectric structures. *Nat Photonics* 7:153–158.
31. Safavi-Naeini AH, et al. (2014) Two-dimensional phononic-photonic band gap optomechanical crystal cavity. *Phys Rev Lett* 112:153603.
32. Maldovan M (2013) Sound and heat revolutions in phononics. *Nature* 503:209–217.
33. Popa B-I, Zigoneanu L, Cummer SA (2011) Experimental acoustic ground cloak in air. *Phys Rev Lett* 106:253901.
34. Adibi A, Khelif A (2016) *Phononic Crystals: Fundamentals and Applications* (Springer, New York).
35. Ma G, Sheng P (2016) Acoustic metamaterials: From local resonances to broad horizons. *Sci Adv* 2:e1501595.
36. Neto AHC, Guinea F, Peres NMR, Novoselov KS, Geim AK (2009) The electronic properties of graphene. *Rev Mod Phys* 81:109–162.
37. Brey L, Fertig HA (2006) Edge states and the quantized hall effect in graphene. *Phys Rev B* 73:195408.
38. Lu L, Joannopoulos JD, Soljacic M (2014) Topological photonics. *Nat Photonics* 8: 821–829.
39. Balram KC, Davanço MI, Song JD, Srinivasan K (2016) Coherent coupling between radiofrequency, optical and acoustic waves in piezo-optomechanical circuits. *Nat Photonics* 10:346–352.